PNAS RESEARCH ARTICLE | ENGINEERING

Adjustable object floating states based on three-segment three-phase contact line evolution

An Li[a,b,c,d], Huizeng Li[a,c,d,1], Zhipeng Zhao[a,b,c,d], Luanluan Xue[a,b,c,d], Zheng Li[a,c,d], Kaixuan Li[a,b,c,d], Mingzhu Li[a,b,c,d], and Yanlin Song[a,b,c,d,1]

Edited by David Weitz, Harvard University, Cambridge, MA; received February 3, 2022; accepted February 21, 2022

Objects floating on water are ubiquitous in nature and daily life. The floating states of objects are significant for a wide range of fields, including assembly, mineral flotation, nanostructured construction, and floating robot design. Generally, an object exhibits a unique and fixed floating state. The real-time regulation of floating states by a simple method is attractive but challenging. Based on in-depth analysis of the different floating states of fruits falling on water, we reveal that the mutable floating states are caused by the three-segment three-phase contact line dynamics. Accordingly, we propose a "buoyancy hysteresis loop" for the transformation of objects between different floating states. More importantly, we demonstrate the potential applications of floating state transformation in solar-powered water evaporation and interface catalysis. The evaporation and catalytic efficiencies can be changed several times by switching the floating state. These findings deepen the understanding of the interfacial effect to the floating of micro-objects and show great potential for floating-related fields.

interfacial effect | floating state regulation | floating robot

Significance

Adjusting the floating states when objects float on water shows great potential for assembly, mineral flotation, nanostructured construction, and floating robot design, but the real-time regulation of floating states is challenging. Inspired by the different floating states of a falling fruit, we propose a facile strategy to transform the object between different floating states based on a three-segment three-phase contact line evolution. In addition, the potential of floating state transformation in solar-powered water evaporation, interface catalysis, and drug delivery is demonstrated. These findings provide insights into floating regulation and show great potential for floating-related applications.

Objects floating on the fluid interface are crucial for various applications (1–6). For example, porous materials floating on water surfaces show great potential in oil spill remediation (7, 8) and solar-driven steam production (3, 9, 10), and the assembly of microparticles on the air/water or oil/water interface is widely exploited for emulsification (11, 12) and fabrication of superarchitectures (13, 14). After Archimedes' law revealed the effect of hydrostatic pressure on the floating state, the influence of material surface properties on the floating state has been recognized in recent decades (15–17). Especially for small floating objects at the scale of centimeters or millimeters, the influence of surface properties might become more dominant than buoyancy, with typical examples including water striders and alkali flies, whose superhydrophobic legs produce adequate surface tensions (10 times greater than buoyancy) to help them slide on the water surface (18, 19). In these studies, surface tension exerts a fixed effect on the floating objects. Considering the fixed morphology and chemical property, it is generally believed that a floating object exhibits a single and unique floating state.

To regulate floating states, the hydrophobization or hydrophilization of the material surface through chemical vapor deposition, plasma treatment, and laser etching are typically used, which undeniably complicates the manufacturing (20–25). Here, we realize the transformation of an object between different floating states under the guidance of a "buoyancy hysteresis loop" and reveal the mechanism of the mutable floating states as the three-segment three-phase contact angle evolution (pinning–slipping–pinning). Moreover, we demonstrate the applications of the controllable floating state in controlling solar-powered water evaporation, interface catalysis, and drug release. These findings will deepen the understanding of the interfacial effect on floating objects and provide a strategy to regulate the floating state.

Results

Mutable Floating States of Objects. We demonstrate that the fruits of *Ardisia crenata*, a kind of shrub that prefers to disperse seeds by water flow (26), display different floating states when falling on the water surface from different heights (Movie S1). To eliminate the influences from the weight and the shape of the fruits, we repeatedly drop the same fruit on water and measure the immersion depths (Fig. 1*A*). As shown in Fig. 1 *B* and *C*, after falling, the fruit dropped from a height of 1 cm shows a large immersion depth (6.1 mm) and a small contact angle (70°) compared with the 0.5–cm-dropped fruit that has a small immersion depth (5.1 mm) and a large contact angle (102°). The results indicate that the fruit can display different floating states and buoyancies when falling from different heights.

Author affiliations: [a]Key Laboratory of Green Printing, Institute of Chemistry, Chinese Academy of Sciences (ICCAS), Beijing 100190, People's Republic of China; [b]School of Chemical Sciences, University of Chinese Academy of Sciences, Beijing 100049, People's Republic of China; [c]Beijing Engineering Research Center of Nanomaterials for Green Printing Technology, Beijing 100190, People's Republic of China; and [d]Beijing National Laboratory for Molecular Sciences (BNLMS), Beijing 100190, People's Republic of China

Author contributions: A.L., H.L., and Y.S. designed research; A.L. performed research; L.X. and Y.S. contributed new reagents/analytic tools; A.L., H.L., Z.Z., Z.L., K.L., M.L., and Y.S. analyzed data; and A.L., H.L., M.L., and Y.S. wrote the paper.

The authors declare no competing interest.

This article is a PNAS Direct Submission.

[1]To whom correspondence may be addressed. Email: lihz@iccas.ac.cn or ylsong@iccas.ac.cn.

This article contains supporting information online at http://www.pnas.org/lookup/suppl/doi:10.1073/pnas.2201665119/-/DCSupplemental.

Published March 22, 2022.

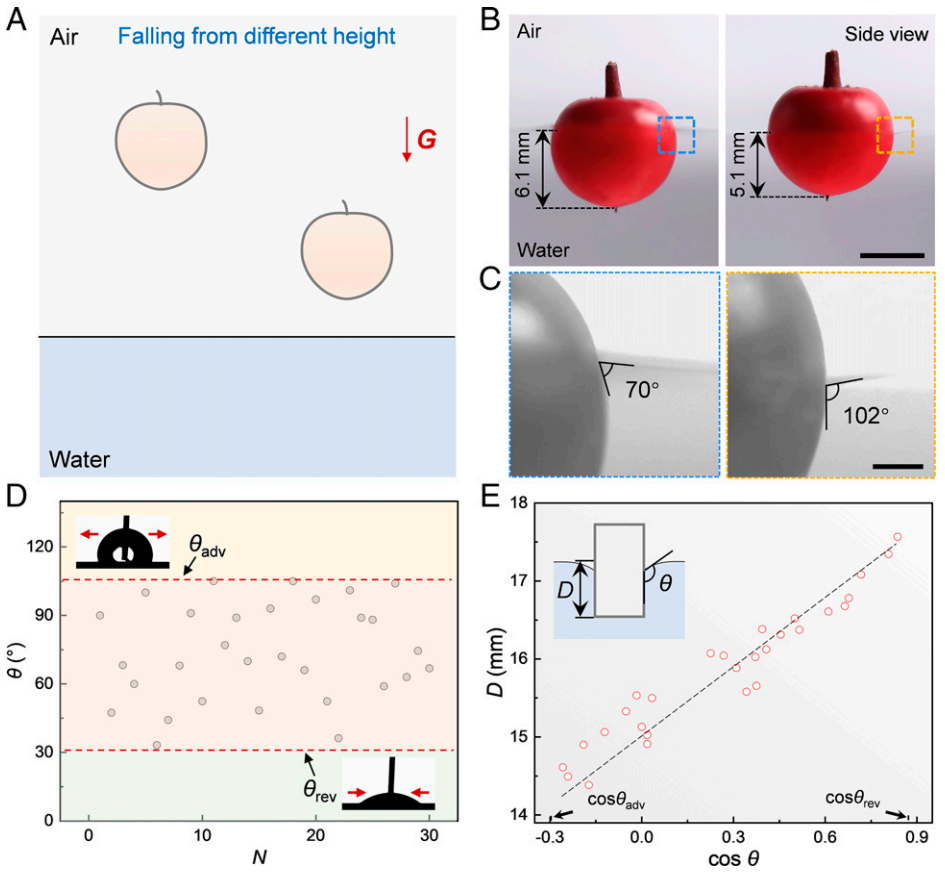

Fig. 1. *A. crenata* fruits exhibit mutable floating states. (*A*) Scheme of fruit falling on the water from different heights; *G*, gravity. (*B* and *C*) The same fruit falling from different heights shows different immersion depths and contact angles. (Scale bars in *B* and *C*, 5 mm and 2 mm, respectively.) (*D*) Distribution range of contact angle θ. The contact angle is obtained by dropping a cuboid box in water 30 times. The red dashed lines are the receding contact angle (θ_{rev}, 33°) and the advancing contact angle (θ_{adv}, 115°). (*E*) Plot of the immersion depth *D* versus the exhibited contact angle θ (red dots). The contact angle and the immersion depth are measured when the box is stabilized. The calculated data are shown by the black dashed line.

For verification, we performed 30 independent dropping and flotation tests using a cuboid box that has a uniform morphology and surface property to make the results more controllable and reliable (Movie S2). Detailed parameters and mutable floating states of the box are shown in *SI Appendix*, Fig. S1. As shown in Fig. 1 *D* and *E*, the results clearly manifest the mutable floating states and buoyancies of the box. Interestingly, we find that the contact angles of the box lie in the range of 33° to 115°, which are exactly the receding and the advancing contact angles of the box surface (27). In addition, unlike the physical aging of the three-phase contact line (TCL) on floating particles (28), the linearly increased immersion depth with the contact angle fits well with the force balance curve (the black dashed line), indicating that the floating box is in an equilibrium state (29) (*SI Appendix*, Fig. S2). The results indicate that objects can indeed exhibit mutable floating states and buoyancies even in force equilibrium. Actually, the phenomenon of variable floating states and buoyancies are widely existed in daily life, as demonstrated in *SI Appendix*, Fig. S3.

Analysis of the Falling Process. We explored how the falling process affects the stable floating state. A high-speed camera was used to record the box-falling dynamics, as displayed in Movie S3. When releasing the box on the water surface, it falls into water and then floats up. The falling–floating vibration (Fig. 2*A*) lasts about 30 s before the stable floating. During the vibration process, the real-time contact angle obtained from the side view varies periodically with time, as shown by the sequenced images in Fig. 2*B* and the plot in Fig. 2*C*. When the box starts to fall, the contact angle first increases from 107° to the advancing contact angle of 115° (0 to 67 ms) and then remains at 115° in the further falling (67 to 170 ms). Subsequently, the contact angle varies as the box floats up and down but will not reach the advancing or receding contact angles (Movie S4).

In this process, the TCL exhibits a three-segment evolution of pinning–slipping–pinning, as shown in Fig. 2*D*, *Top*. In addition, the TCL slip distance varies with the falling height. This can be explained by the following. When releasing the box, its gravity is larger than the buoyancy and solid–liquid adhesion, resulting in the box falling downward with the TCL pinned (0 to 67 ms). Then, the increase in contact angle enlarges the solid–liquid adhesion until reaching the maximum solid–liquid adhesion at the advancing contact angle. In this process, the TCL slips for a distance, and the box velocity reduces to zero (67 to 170 ms). The large falling height contributes to a large slip distance. During the subsequent floating up, the upward inertia is not large enough to overcome the resistance from gravity and solid–liquid adhesion, and the TCL remains pinned. The pinning of TCL lasts until reaching stable floating. Therefore, we can conclude that the three-segment behavior of the TCL dynamics, caused by the solid–liquid adhesion, is the origin of the different floating states of the object. For verification, we dropped a superhydrophobic box on water, and there was only a two-segment TCL evolution (pinning and slipping) before reaching stabilization (Fig. 2*D*, *Bottom*, and *SI Appendix*, Fig. S4). As a result, the

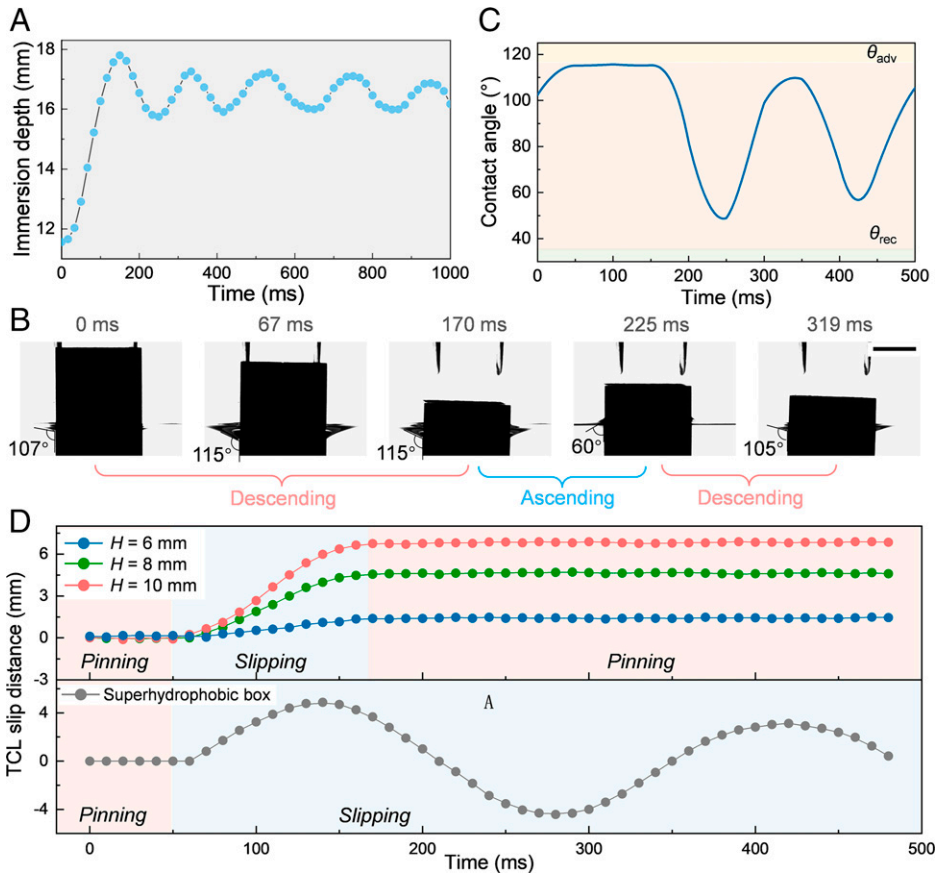

Fig. 2. Dynamic process of falling. (*A*) Curve of immersion depth versus time. (*B*) Snapshots of the box falling on the water. (Scale bar, 5 mm.) (*C*) Curve of contact angle versus time. (*D*) TCL dynamics of the boxes falling from different heights.

superhydrophobic box only shows a certain floating state even when released from different heights (*SI Appendix*, Fig. S5). Similar behaviors appear when the raspberry, a kind of superhydrophobic fruit, falls from different heights and shows an identical floating state (*SI Appendix*, Fig. S6). Detailed analysis of the falling dynamics is provided in SI Appendix, *Supplementary Information Text*.

Buoyancy Hysteresis Loop. Diverse floating states can be realized by falling from different heights, but this method has great limitations. The above analysis of the mechanism, the three-segment TCL evolution, inspired us to propose a simple and effective strategy to adjust the floating state. As the floating state relates to the TCL slipping distance, we can control the TCL slipping using a loading−unloading cycle (30) and achieve transformation of the object between different floating states. Fig. 3*A* shows the scheme of the apparatus, in which a box is held by a platform that can apply periodical force to the box. The force balance on the box is $mg + F = F_b - 4\gamma a\cos\theta$, where F is the applied force (Fig. 3*A*), a is the side length of the box, and F_b is the buoyancy and can be obtained by the immersion depth D from $F_b = \rho g a^2 D$. Variation of the buoyancy versus the applied periodical force is shown in Fig. 3*B*. During the loading−unloading cycle (i to ii to iii), the change of the buoyancy first equals and then lags behind the change of the applied force. Meanwhile, the TCL first slips (i to ii) and then remains pinned (ii to iii). A similar behavior appears in the unloading−loading cycle (iii to iv to i), forming a rhombic loop that is named the buoyancy hysteresis loop (Movie S5). The contact angles further confirm the TCL evolution during the loading−unloading cycles (*SI Appendix*, Fig. S7).

The buoyancy hysteresis loop provides general guidance to alter the TCL position and, more importantly, to adjust the floating states of objects. For example, the first loading–unloading cycle transforms the floating object from a small-immersion state to a large-immersion state, while the first unloading–loading cycle transforms the floating object from a large-immersion state to a small-immersion state. In addition, the loop can be used to evaluate the influence of the mutable floating states on the floating objects. We find that enlarging the width of the box narrows the loop, while diminishing the width contributes to a wide loop (*SI Appendix*, Fig. S8). This is because the shape of the buoyancy hysteresis loop is determined by the slope of ii to iii section (or iv to I section), which is denoted by k. A negative relationship exists between k and the object perimeter/cross-section area ratio ε, that is, $1/k \sim \gamma\varepsilon/\rho g l_c$ (here, $\varepsilon = 4a/a^2$ for the cuboid box), explaining why the mutable floating state is easy to observe in small objects and can often be ignored in large ones. As shown in Fig. 3*C*, the experimental data (dots) are well fitted with the theoretical results (dashed line), suggesting the validity of this evaluation method. Furthermore, the disappeared loops of superhydrophilic and superhydrophobic boxes confirm the effect of the TCL evolution on the mutable floating states, as shown in *SI Appendix*, Fig. S9.

Without complex surface treatments, our research shows a simple way to adjust the floating states. For demonstration, we designed a floating-adjustable robot that can switch between surface state and dive state. As shown in Fig. 3*D*, a cylindrical magnet is placed inside the semiellipsoidal robot; thus, a downward or upward force can be applied to the robot when using another magnet to approach the robot from the top or the bottom (*SI Appendix*, Fig. S10). The advancing and receding contact angles of the robot surface are 115° and 70°,

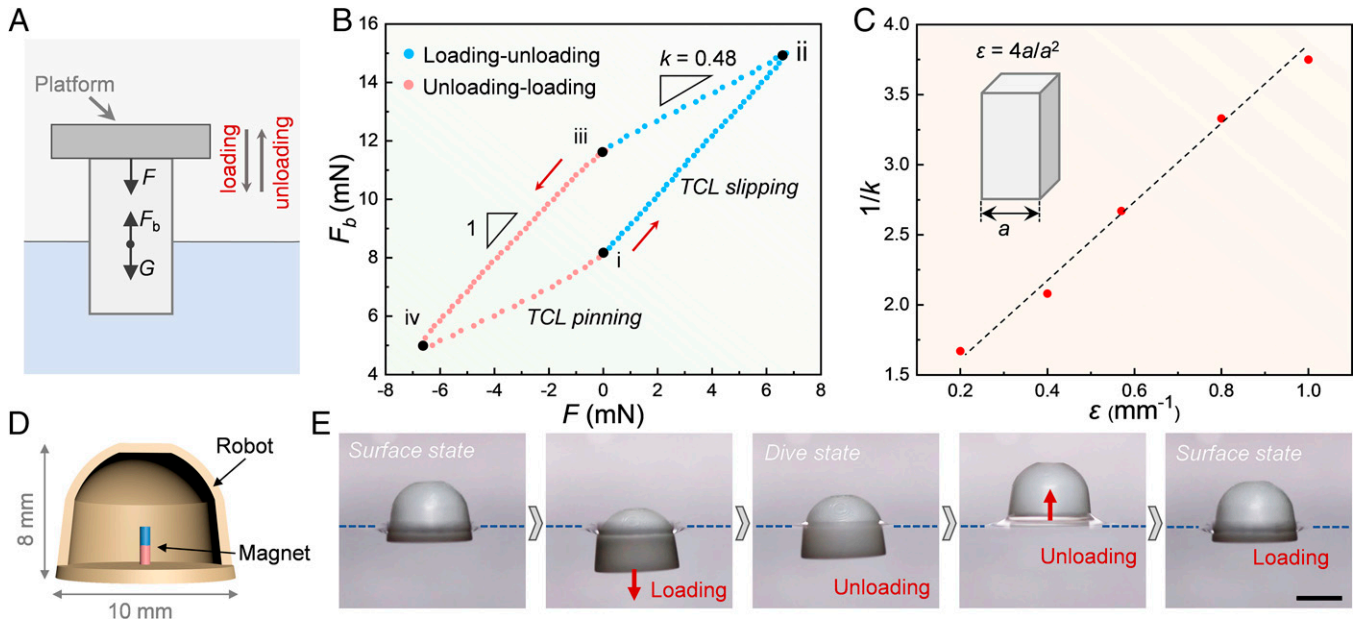

Fig. 3. Buoyancy hysteresis loop. (*A*) Schematic of the apparatus. A cuboid box is fixed under a platform, which can slowly apply force to the box. The box is subjected to the buoyancy F_b, the surface tension F_s, the gravity *G*, and the applied force *F*. (*B*) Variation of the buoyancy with the applied force during the loading−unloading (i to ii to iii) and unloading−loading (iii to iv to i) cycles. The buoyancy lags behind the applied force in the sections of ii to iii and iv to i, resulting in a rhombic loop. (*C*) Dependence of 1/*k* on the box's perimeter/cross-section area ratio ε. The theoretical prediction is plotted with a black dashed line. (*D*) Illustration of the floating robot. (*E*) Surface state and dive state of the robot. A loading−unloading process sinks the robot to dive state with a large buoyancy. An unloading−loading process can float the robot up to a surface state. (Scale bar, 5 mm.).

respectively. According to the buoyancy hysteresis loop, the first loading–unloading cycle makes the robot sink and finally stabilize with a large immersion, turning the robot into a dive state. By contrast, the first unloading–loading process reverts the robot to a surface state with a small immersion depth (Fig. 3*E* and Movie S6). Based on this, the autonomous interface collection and locomotion are realized, as demonstrated in *SI Appendix*, Fig. S11, and Movies S7 and S8.

Applications of the Mutable Floating States. The floating state of an object determines the contact and wetting of liquid on the solid surface. Therefore, the adjustment of the floating states can exert significant influence on the interfacial-related application. In the following, we take controllable water evaporation, interfacial catalysis, and drug release as examples for illustration. Solar-powered water evaporation, which can evaporate water at the surface using solar energy, has shown promising prospects in clean water production and water treatment (31). Here, we find that accelerating or slowing evaporation can be easily achieved by adjusting the floating state of the solar-heated floaters. The carbon black–coated foam particles are used as solar-heated floaters for evaporation. Carbon black has been proven to effectively convert solar power into heat, and the foam core prevents the thermal conduction between the heated carbon black and water (32, 33). As shown in Fig. 4 *A*–*C*, when placing at surface state, the floaters prevent both the direct illumination of the water surface and the contact between the solar-heated areas with water. Hence, the heat insulation effect reduces water evaporation. Conversely, adjusting the floaters to dive state results in the illumination of water and the direct contact of the solar-heated areas with water to accelerate evaporation. The infrared images of the different floating-state floaters at the simulated solar illumination (1 kW m^{-2}) confirm the mechanism of accelerating or slowing evaporation, as shown in Fig. 4 *D* and *E*. Under this circumstance, the evaporation efficiency of the floaters at dive state reaches 0.9 kg m^{-2} h^{-1}, while the floaters at surface state reduce the efficiency to 0.15 kg m^{-2} h^{-1} (Fig. 4*F*). Fig. 4*G* demonstrates the different evaporation efficiencies of the floaters at different floating states by illuminating the floater-covered water at 1 kW m^{-2} for 3 h.

In addition, we demonstrate the controllable interface catalysis using a platinum metal-coated polypropylene bead to catalyze the decomposition of hydrogen peroxide. As shown in Fig. 4*H*, controlling the floating state of the bead contributes to different contact areas between platinum and hydrogen peroxide, which results in diverse catalytic efficiencies. We estimated the catalytic efficiency of the two states by calculating the number and volume of the generated bubbles and found that the catalytic efficiency of the dive-state bead (Fig. 4*J*) is about three times higher than that of the surface-state bead (Fig. 4*I* and Movie S9). In addition, the different drug-release capabilities by transforming the capsule floating state are realized, as displayed in *SI Appendix*, Fig. S12.

Discussion

In this work, we illustrate how three-segment TCL evolution induces the mutable floating states of objects. More importantly, we propose the buoyancy hysteresis loop and achieve facile and efficient transformation of the objects between different floating states through loading−unloading cycles. Moreover, we fabricate different floating-adjustable floaters that show great potential for applications, such as autonomous interface collection, innovative floating robots, controllable drug delivery, interface catalysis, and solar-powered water evaporation.

Materials and Methods

Preparation of *A. crenata* Fruits. The fruits used in Fig. 1 are similar in weight and size. After being picked up from the *A. crenata*, the fruits were washed with ethanol and deionized water and then blown dry with nitrogen. Deionized water was used to float the fruits.

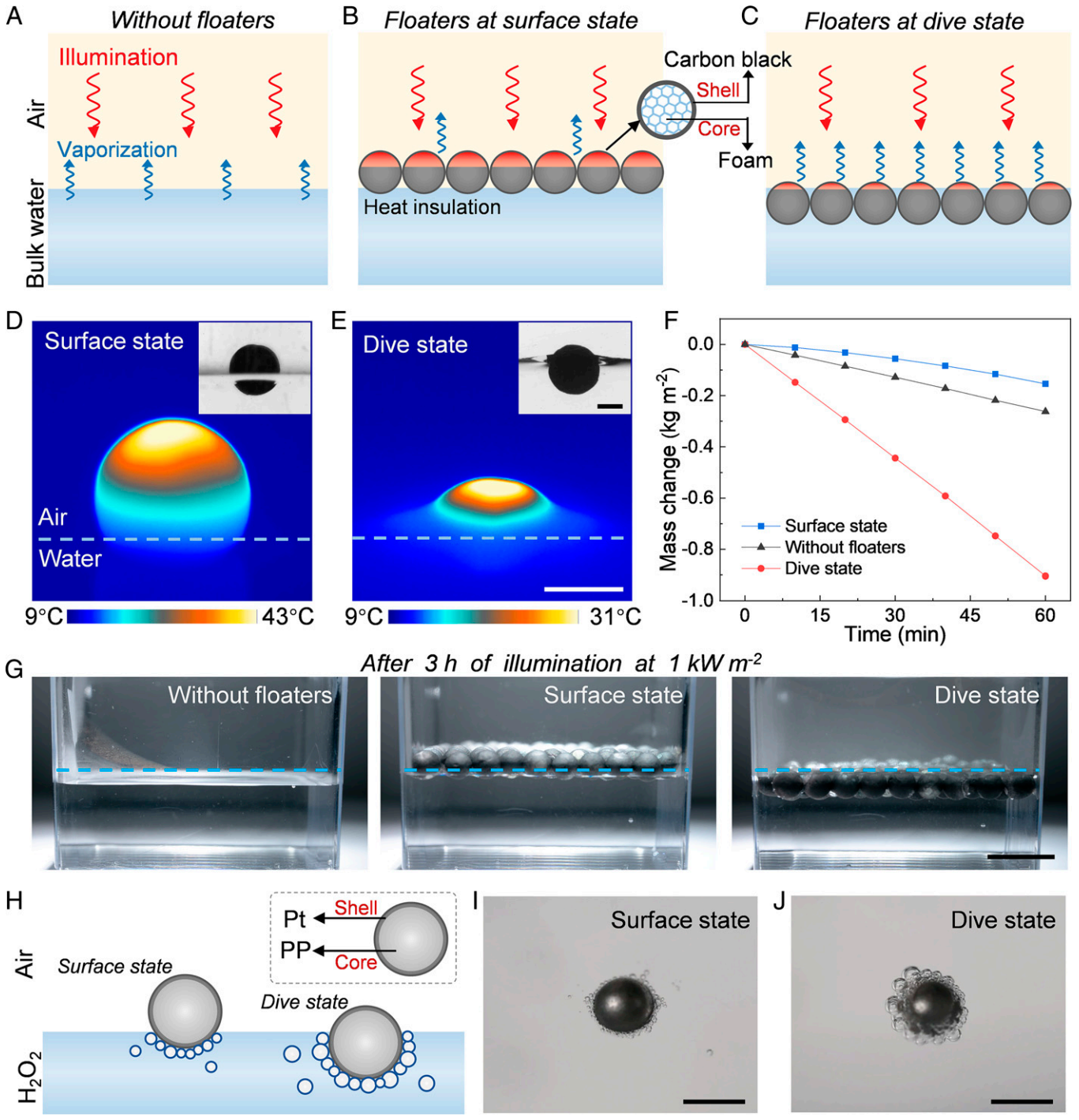

Fig. 4. Applications of the transform of object floating states. (*A*–*C*) Schemes of the water evaporation control strategy by solar-heated floaters with different states. (*D* and *E*) Infrared images of floaters at surface state (*D*) and dive state (*E*). Inset images are the optical photos of the floater at different states. (Scale bars, 2 mm.) (*F*) Mass change curves of water covered by different state floaters. (*G*) Optical photos of water covered by different state floaters after 3 h of illumination. (Scale bar, 10 mm.) (*H*) Scheme of the effect of different floating states on catalysis efficiency. PP: polypropylene, Pt: platinum. (*I* and *J*) Optical photos of the catalytic efficiency of floaters at different floating states. (Scale bars, 2 mm.)

Preparation of the Cuboid Box. The hollow cuboid box used in Fig. 2 was made of 6061 aluminum alloy and processed by a numerical control machine (CNC). The length, width, and height of the box were 10 mm, 10 mm, and 20 mm, respectively. The wall thickness of the hollow box was 0.9 mm. After CNC machining, we used 100-mesh, 200-mesh, 500-mesh, and 1,000-mesh sandpaper to polish the box. Then, the box was washed with ethanol and deionized water and blown dry with nitrogen. To increase the hydrophobicity, the box was modified with 1*H*,1*H*,2*H*,2*H*-perfluorodecyltrimethoxysilane by chemical vapor deposition at 80 °C for 4 h. The equilibrium, advancing, and receding contact angles of the obtained box were 95°, 115°, and 33°, respectively.

Floating Tests for the Buoyancy Hysteresis Loop. The apparatus was composed of a platform and a force sensor. The box was attached to the lower surface of the platform and was preimmersed in water. The initial immersion depth was 8 mm. The contact angle was the advancing contact angle. The platform applied forces to move the box. The applied force can be measured by the force sensor with an accuracy of 1 μN.

Preparation of the Floating-Adjustable Robot. The semiellipsoid robot was made of resin and prepared by three-dimensional printing. The bottom radius was 5 mm, the height was 8 mm, and the wall thickness was 1 mm. The weight

of the robot was 183 mg. The surface of the robot was sequentially polished by 500-mesh, 2,000-mesh, 5,000-mesh, and 10,000-mesh sandpaper, respectively. The advancing and receding contact angles of the robot surface were 115° and 70°, respectively. We placed a micromagnet with a diameter of 1 mm and a height of 3 mm in the robot. The magnetic field intensity of the micromagnet was 14.1 mT. When we controlled a magnet (magnetic field intensity of 64.4 mT) to approach the robot from the bottom, a downward attraction force made the robot sink into the water. The robot remained static at the dive state after the removal of the magnet. Similarly, approaching the magnet to the robot from the top made the robot float up to the water surface. The robot remained static at the surface state after the removal of the magnet. The microfloaters were polypropylene spheres with a diameter of 2.3 mm. The weight of the sphere was 6 mg. When the spheres were gently placed on water, the contact angle was about 105°.

Preparation of the Solar-Heated Floaters. The float was obtained by coating carbon black on commercial spherical polystyrene foam. After drying polystyrene foam immersed from a commercial carbon black solution, a carbon black layer was constructed on the surface of the foam. The diameter of the foam was 4 mm, and the thermal conductivity of porous polystyrene was around 0.04 W m^{-1} K^{-1}. A xenon lamp was used to simulate solar illumination. The mass change of water was measured by using a high-accuracy balance (FA 2004, 0.1 mg in accuracy).

Preparation of the Interface Catalysis. A polypropylene bead coated with platinum metal was used to demonstrate the interface catalysis. The density and diameter of the polypropylene bead were 0.9 g cm^{-3} and 2 mm, respectively. Platinum was sprayed onto polypropylene pellets by vacuum magnetron sputtering. The current was 20 mA, and the time was 300 s. The mass fraction of hydrogen peroxide used in the catalytic experiments was 5%.

Data Availability. All study data are included in the article and/or supporting information.

ACKNOWLEDGMENTS. This work is supported by the National Key R&D Program of China (2018YFA0208501 and 2018YFA0703200), the National Natural Science Foundation of China (numbers 51903240, 51773206, and 51961145102), the Postdoctoral Innovative Talents Support Program (BX20180313), the China Postdoctoral Science Foundation (2018M641482), K. C. Wong Education Foundation, and Beijing National Laboratory for Molecular Sciences (number BNLMS-CXXM-202005).

1. A. Suzuki, E. Ohtani, T. Kato, Flotation of diamond in mantle melt at high pressure. *Science* **269**, 216–218 (1995).
2. J.-B. Gorce *et al.*, Rolling spinners on the water surface. *Sci. Adv.* **7**, eabd4632 (2021).
3. X. Zhou, F. Zhao, Y. Guo, B. Rosenberger, G. Yu, Architecting highly hydratable polymer networks to tune the water state for solar water purification. *Sci. Adv.* **5**, eaaw5484 (2019).
4. B. P. Binks, T. S. Horozov, *Colloidal Particles at Liquid Interfaces* (Cambridge University Press, 2006).
5. G. Xie *et al.*, Hanging droplets from liquid surfaces. *Proc. Natl. Acad. Sci. U.S.A.* **117**, 8360–8365 (2020).
6. X. Wu *et al.*, Ferromagnetic liquid droplets with adjustable magnetic properties. *Proc. Natl. Acad. Sci. U.S.A.* **118**, e2017355118 (2021).
7. J. Ge *et al.*, Pumping through porous hydrophobic/oleophilic materials: An alternative technology for oil spill remediation. *Angew. Chem. Int. Ed. Engl.* **53**, 3612–3616 (2014).
8. J. Ge *et al.*, Joule-heated graphene-wrapped sponge enables fast clean-up of viscous crude-oil spill. *Nat. Nanotechnol.* **12**, 434–440 (2017).
9. H. Li *et al.*, Side area-assisted 3D evaporator with antibiofouling function for ultra-efficient solar steam generation. *Adv. Mater.* **33**, e2102258 (2021).
10. P. D. Dongare *et al.*, Nanophotonics-enabled solar membrane distillation for off-grid water purification. *Proc. Natl. Acad. Sci. U.S.A.* **114**, 6936–6941 (2017).
11. R. McGorty, J. Fung, D. Kaz, V. N. Manoharan, Colloidal self-assembly at an interface. *Mater. Today* **13**, 34–42 (2010).
12. R. Aveyard, B. P. Binks, J. H. Clint, Emulsions stabilised solely by colloidal particles. *Adv. Colloid. Interfac.* **100-102**, 503–546 (2003).
13. D. Jung *et al.*, Highly conductive and elastic nanomembrane for skin electronics. *Science* **373**, 1022–1026 (2021).
14. Z. Hu, W. Fang, Q. Li, X.-Q. Feng, J. A. Lv, Optocapillarity-driven assembly and reconfiguration of liquid crystal polymer actuators. *Nat. Commun.* **11**, 5780 (2020).
15. D. L. Hu, B. Chan, J. W. M. Bush, The hydrodynamics of water strider locomotion. *Nature* **424**, 663–666 (2003).
16. D. L. Hu, J. W. M. Bush, Meniscus-climbing insects. *Nature* **437**, 733–736 (2005).
17. D. Vella, Floating versus sinking. *Annu. Rev. Fluid Mech.* **47**, 115–135 (2015).
18. X. Gao, L. Jiang, Biophysics: Water-repellent legs of water striders. *Nature* **432**, 36–36 (2004).
19. F. van Breugel, M. H. Dickinson, Superhydrophobic diving flies (*Ephydra hians*) and the hypersaline waters of Mono Lake. *Proc. Natl. Acad. Sci. U.S.A.* **114**, 13483–13488 (2017).
20. X. Deng *et al.*, Transparent, thermally stable and mechanically robust superhydrophobic surfaces made from porous silica capsules. *Adv. Mater.* **23**, 2962–2965 (2011).
21. H. Li *et al.*, Heterogeneous wettability surfaces: Principle, construction, and applications. *Small Structures* **1**, 2000028 (2020).
22. F. Rafieian, M. Hosseini, M. Jonoobi, Q. Yu, Development of hydrophobic nanocellulose-based aerogel via chemical vapor deposition for oil separation for water treatment. *Cellulose* **25**, 4695–4710 (2018).
23. F. Chen *et al.*, Stability of plasma treated superhydrophobic surfaces under different ambient conditions. *J. Colloid Interface Sci.* **470**, 221–228 (2016).
24. H. Li *et al.*, Droplet precise self-splitting on patterned adhesive surfaces for simultaneous multidetection. *Angew. Chem. Int. Ed. Engl.* **59**, 10535–10539 (2020).
25. H. Li *et al.*, Spontaneous droplets gyrating via asymmetric self-splitting on heterogeneous surfaces. *Nat. Commun.* **10**, 950 (2019).
26. W. T. Parsons, W. T. Parsons, E. Cuthbertson, *Noxious Weeds of Australia* (CSIRO Publishing, 2001).
27. L. Gao, T. J. McCarthy, Contact angle hysteresis explained. *Langmuir* **22**, 6234–6237 (2006).
28. D. M. Kaz, R. McGorty, M. Mani, M. P. Brenner, V. N. Manoharan, Physical ageing of the contact line on colloidal particles at liquid interfaces. *Nat. Mater.* **11**, 138–142 (2011).
29. D. Vella, D.-G. Lee, H.-Y. Kim, The load supported by small floating objects. *Langmuir* **22**, 5979–5981 (2006).
30. D. Guan, E. Charlaix, P. Tong, State and rate dependent contact line dynamics over an aging soft surface. *Phys. Rev. Lett.* **124**, 188003 (2020).
31. F. Zhao, Y. Guo, X. Zhou, W. Shi, G. Yu, Materials for solar-powered water evaporation. *Nat. Rev. Mater.* **5**, 388–401 (2020).
32. N. Xu *et al.*, A scalable fish-school inspired self-assembled particle system for solar-powered water-solute separation. *Natl. Sci. Rev.* **8**, nwab065 (2021).
33. J. Yuan *et al.*, 3D-printed hierarchical porous cellulose/alginate/carbon black hydrogel for high-efficiency solar steam generation. *Chem. Eng. J.* **430**, 132765 (2022).